Chinese Chemical Letters 37 (2026) 112286

Contents lists available at ScienceDirect

Chinese Chemical Letters

journal homepage: www.elsevier.com/locate/cclet

Plasma-induced oxygen vacancy on Co_3O_4 for enhanced singlet oxygen generation *via* peroxymonosulfate activation

Keyi Gao[a], Yunbo Wu[b], Shulin Shen[a], Dawei Wang[a], Yilan Jiang[a,*]

[a] *Key Laboratory of Integrated Regulation and Resource Development on Shallow Lake of Ministry of Education, College of Environment, Hohai University, Nanjing 210098, China*

[b] *Jiangsu Academy of Environmental Industry and Technology Corporation, Nanjing 210019, China*

ARTICLE INFO

Article history:
Received 19 August 2025
Revised 23 October 2025
Accepted 15 December 2025
Available online 15 December 2025

Keywords:
Plasma treatment
Oxygen vacancy
Cobalt-based oxide
Peroxymonosulfate activation
Singlet oxygen

ABSTRACT

In this study, a simple N_2 plasma strategy was employed to modify the surface of Co_3O_4, significantly enhancing its efficiency in activating peroxymonosulfate (PMS) for the degradation of tetracycline hydrochloride (TC). Co_3O_4 treated with plasma for 30 min (Co_3O_4–30) achieved a TC degradation efficiency of 93.2 % within 30 min ($k = 0.078$ min^{-1}), which was significantly higher than that of the pristine Co_3O_4 ($k = 0.023$ min^{-1}). Studies demonstrated that plasma treatment induced the generation of oxygen vacancies (O_v) on the surface of Co_3O_4, which serve as key active sites during the catalytic process and facilitate the adsorption of PMS to generate singlet oxygen ($^1O_2$). As the dominant reactive oxygen species, the steady-state concentration of $^1O_2$ was positively correlated with the TC degradation rate. Additionally, dominated by the non-radical pathway, the PMS/Co_3O_4–30 system exhibited high selectivity toward electron-rich pollutants as well as strong anti-interference capability against anions and complex water matrices. This study demonstrates that plasma technology serves as a viable approach for defect engineering in catalysts, enabling the selective generation of $^1O_2$ from PMS.

© 2026 Published by Elsevier B.V. on behalf of Chinese Chemical Society and Institute of Materia Medica, Chinese Academy of Medical Sciences.

Antibiotics persist in aquatic environments, posing threats to ecosystems and human health due to hazards such as bioaccumulation and induction of antimicrobial resistance [1,2]. In recent years, persulfate-based advanced oxidation processes (PS-AOPs) have demonstrated remarkable efficiency in degrading organic pollutants [3–5]. As common reactive oxygen species (ROS) in SR-AOP systems, sulfate radical ($SO_4^{\bullet-}$) and hydroxyl radical ($^{\bullet}OH$) achieve high mineralization rates for contaminants owing to their high redox potential and relatively long half-life [6]. However, in complex aqueous matrices, these radicals are readily scavenged, compromising oxidation performance. In contrast, the non-radical pathway dominated by singlet oxygen ($^1O_2$) offers superior selectivity, anti-interference capacity and mild oxidation [7–9]. How to achieve the directional generation of $^1O_2$ in PS-AOPs through the structural regulation of materials is a current research hotspot.

Cobalt-based oxides, exemplified by Co_3O_4, demonstrate significant catalytic potential in water treatment. Oxygen vacancies (O_v), formed by the departure of lattice oxygen atoms from metal oxides, are recognized as effective active sites for activating peroxymonosulfate (PMS) to generate $^1O_2$ [10–12]. During catalysis, O_v typically functions as electron acceptors, adsorbing PMS to initiate intermediate species (*e.g.*, superoxide radicals, $O_2^{\bullet-}$) that subsequently facilitate $^1O_2$ production *via* chain reactions [13,14]. Conventional strategies for creating O_v in metal oxides—including ion doping, chemical reduction, and hydrothermal treatment—although effective, still face challenges such as high synthesis temperature requirements and impure products [15–17]. In contrast, plasma etching emerges as a distinct approach, enabling rapid surface defect formation at ambient temperature through interactions with reductive active species or electrons. This technique offers advantages of low energy consumption and minimal byproduct generation [18,19]. Therefore, plasma treatment provides a promising way to construct surface O_v on Co_3O_4, which may facilitate PMS to generate $^1O_2$.

In this study, Co_3O_4 was treated with N_2 plasma for different durations at room temperature to synthesize O_v-rich Co_3O_4-x (x denotes the reaction time). Comprehensive characterizations *via* X-ray photoelectron spectroscopy (XPS), Raman spectroscopy, and solid-state electron spin resonance (ESR) confirmed the successful introduction of O_v. Co_3O_4-x/PMS systems exhibited significantly enhanced catalytic oxidation performance compared to the pristine-Co_3O_4/PMS system. Probe experiments confirmed that this enhancement was primarily attributed to the facilitated generation of $^1O_2$, whose steady-state concentration exhibited a signifi-

* Corresponding author.
E-mail address: yljiang@hhu.edu.cn (Y. Jiang).

https://doi.org/10.1016/j.cclet.2025.112286
1001-8417/© 2026 Published by Elsevier B.V. on behalf of Chinese Chemical Society and Institute of Materia Medica, Chinese Academy of Medical Sciences.

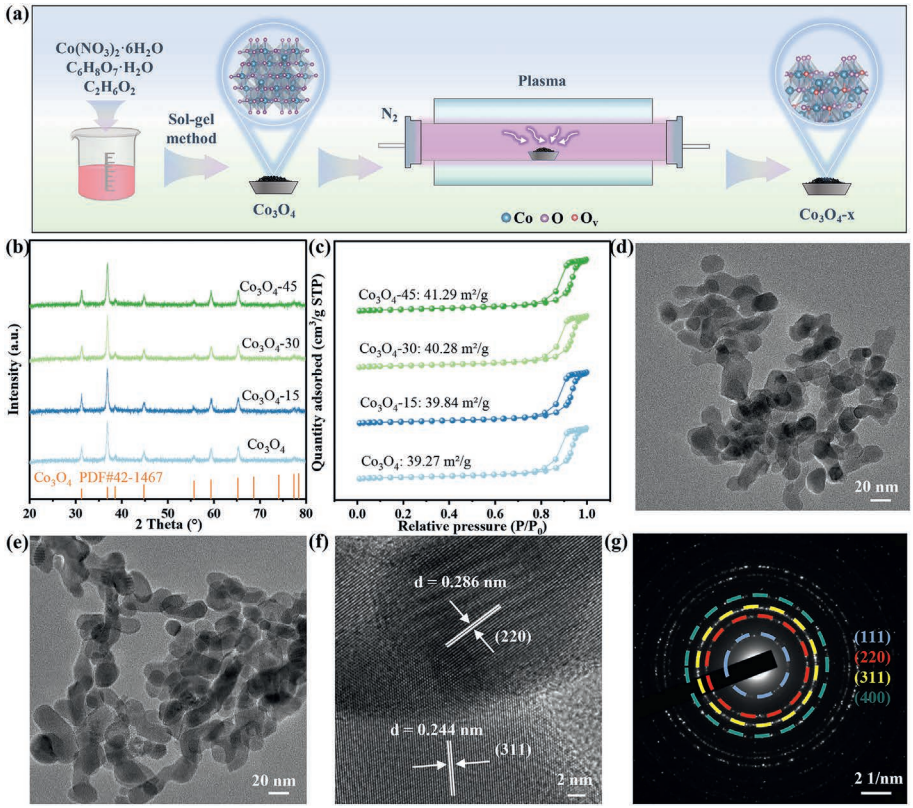


Fig. 1. (a) Synthetic procedure for Co_3O_4-x. (b) XRD patterns of Co_3O_4-x. (c) N_2 adsorption/desorption isotherms. TEM images of (d) Co_3O_4 and (e) Co_3O_4–30. (f) HRTEM image and (g) SAED image of Co_3O_4–30.

cant positive correlation with the improved TC degradation rates. As expected, the incorporation of O_v is shown to be effective in promoting the generation of $^1O_2$. Additionally, Co_3O_4-*x* exhibited excellent stability, reusability, and promising applicability in complex water matrices.

The synthesis procedure is illustrated in Fig. 1a. Pristine Co_3O_4 was prepared *via* the sol-gel method, followed by thermal treatment in a muffle furnace at 400 °C for 2 h. Subsequently, Co_3O_4 were subjected to plasma treatment under a N_2 atmosphere to obtain Co_3O_4-*x* ($x = 15$, 30, 45 min). The phase purity and crystallinity of all samples were confirmed by X-ray diffraction (XRD), as their patterns (Fig. 1b) exhibited diffraction peaks matching well with the standard pattern of Co_3O_4 (PDF #42–1467) [20]. Furthermore, energy-dispersive X-ray spectroscopy (EDS) mapping images (Fig. S1 in Supporting information) clearly demonstrated the homogeneous distribution of Co and O elements across the material surface. Scanning electron microscopy (SEM) images (Fig. S2 in Supporting information) revealed that all samples exhibit irregular bulk morphologies. Notably, increased surface roughness and porosity of Co_3O_4-*x* were observed, attributable to high-energy bombardment induced by plasma. This morphological change was further substantiated by Brunauer-Emmett-Teller (BET) surface area analysis (Fig. 1c), which showed a gradual increase in the specific surface area of Co_3O_4-*x* with prolonged plasma treatment time. At the microscopic scale, however, comparison of the Transmission electron microscope (TEM) images between pristine Co_3O_4 and Co_3O_4–30 revealed comparable morphologies (Figs. 1d and e). High resolution transmission electron microscope (HRTEM) imaging of Co_3O_4–30 (Fig. 1f) further resolved its crystalline nature, displaying distinct lattice fringes with spacings of 0.286 nm and 0.244 nm, corresponding to the (220) and (311) planes of the Co_3O_4 spinel structure, respectively [21]. Additionally, the selected-area electron diffraction (SAED) pattern (Fig. 1g) confirmed the good match between the Co_3O_4-*x* and standard Co_3O_4 [22], indicating that the plasma treatment did not alter the crystal structure of the material.

Solid ESR was employed to detect O_v in pristine Co_3O_4 and Co_3O_4–30 (Fig. S3 in Supporting information). Compared to pristine Co_3O_4, Co_3O_4–30 exhibited a more pronounced ESR signal at a *g*-factor of 2.003, confirming the successful introduction of O_v [23]. The result was further substantiated by Raman scattering. Each sample exhibited four Raman active modes (F_{2g}, E_g, $F_{2g}{}^2$, A_{1g}), corresponding to the crystal cube Co_3O_4 [24,25]. The Raman peak intensity of Co_3O_4-*x* weakened and shifted towards lower frequencies (Fig. 2a). Among them, the A_{1g} peak (685 cm^{-1}) associated with the Co-O bond stretching of the octahedral locus showed a relatively significant redshift change, indicating that plasma treatment altered the local electron density and lattice vibration frequency of the Co_3O_4-*x*, revealing the introduction of O_v [26]. Furthermore, XPS was performed to monitor the valence state distribution and electronic structure of the samples. The O 1s spectra included three distinct peaks (Fig. 2b): Lattice oxygen (O_{latt}, ~530.02 eV), adsorbed oxygen species (O_{ads}, ~531.38 eV), and surface hydroxyl groups/water (O_{H_2O}, ~533.38 eV) [27–29]. O_{ads} is commonly used as a relative indicator for O_v concentration. The relative content of O_{ads} in Co_3O_4–30 (48.91 %) was significantly higher than that in Co_3O_4 (28.98 %) (Fig. 2c), confirming the increased concentration of O_v on the surface of Co_3O_4–30. The Co 2p spectra (Fig. 2d) could be deconvoluted into characteristic peaks corresponding to Co^{2+} (binding energies at 781.89 eV and 796.66 eV) and Co^{3+} (binding energies at 780.06 eV and 795.03 eV) [25]. Compared to the pristine Co_3O_4, the Co^{2+}/Co^{3+} ratio in Co_3O_4–30 increased from 0.48 to 0.68. The decrease in the average valence state of cobalt is attributed to the transfer of electrons from the O atoms to the Co d-bond center during the formation of O_v [30].

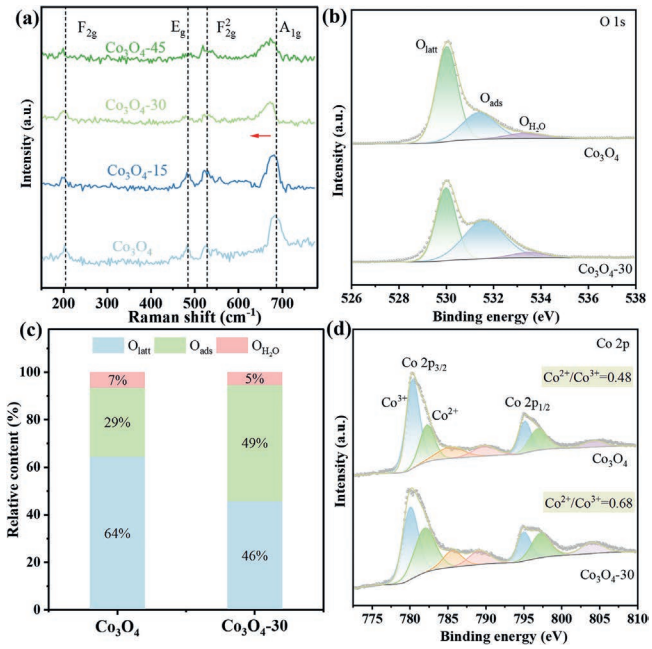


Fig. 2. (a) Raman spectra of Co_3O_4, Co_3O_4–15, Co_3O_4–30 and Co_3O_4–45. (b) O 1s XPS spectrum of Co_3O_4 and Co_3O_4–30. (c) Corresponding proportion of different O species in Co_3O_4 and Co_3O_4–30. (d) Co 2p XPS spectrum of Co_3O_4 and Co_3O_4–30.

The performance of different catalysts for PMS activation was further evaluated. As shown in Fig. 3a, direct PMS oxidation contributed negligibly to TC removal (<1%). Although the physical adsorption performance improved slightly with the increase of plasma treatment duration, the adsorption capacity was still very limited (Fig. S4 in Supporting information). In the oxidative degradation stage, the Co_3O_4-*x*/PMS systems exhibited significantly higher TC degradation efficiency than the pristine Co_3O_4/PMS system (Fig. S5 in Supporting information). Specifically, the Co_3O_4/PMS system only achieved 58.9% TC removal within 30 min, with a first-order reaction kinetic constant (k) of 0.023 min^{-1}. In contrast, the Co_3O_4–15/PMS, Co_3O_4–30/PMS, and Co_3O_4–45/PMS systems demonstrated markedly improved performance, attaining removal efficiencies of 84.7% ($k = 0.055$ min^{-1}), 93.2% ($k = 0.078$ min^{-1}), and 92.7% ($k = 0.077$ min^{-1}), respectively. The catalytic activity of Co_3O_4-*x* was significantly enhanced with longer plasma processing time. Given the nearly identical performance of Co_3O_4–30 and Co_3O_4–45, it can be inferred that a 30 min-plasma treatment is sufficient to achieve complete formation of O_v on the surface of Co_3O_4. Besides, key parameters of reaction (PMS dosage, catalyst dosage, pH and TC dosage) were optimized to establish the best degradation conditions (Fig. S6 in Supporting information). Moreover, Comparison of the performance with advanced catalysts in recent researches demonstrated the superior activity of Co_3O_4–30 for TC degradation *via* PMS activation (Fig. S7 and Table S1 in Supporting information).

To identify the dominant ROS, quenching experiments and ESR measurements were performed. As shown in Fig. 3b, the impact of *tert*–butanol (TBA, $k_{TBA, \cdot OH} = 6.0 \times 10^8$ L mol^{-1} s^{-1}) and methanol (MeOH, k_{MeOH}, $SO_4^{\cdot-} = 1.1 \times 10^7$ L mol^{-1} s^{-1}, $k_{MeOH, \cdot OH} = 9.7 \times 10^8$ L mol^{-1} s^{-1}) on TC degradation was relatively weak [31,32]. Meanwhile, no significant signal peaks corresponding to DMPO-$SO_4^{\cdot-}$ or DMPO-$^{\cdot}$OH were observed (Fig. S8a in Supporting information), suggesting that the production of $SO_4^{\cdot-}$ and $^{\cdot}$OH radicals (p-BQ, $k_{p\text{-}BQ, O_2^{\cdot-}} = 8.3 \times 10^8$ L mol^{-1} s^{-1}) and furfuryl alcohol (FFA, $k_{FFA, {}^1O_2} = 1.2 \times 10^8$ L mol^{-1} s^{-1}) to the Co_3O_4–30/PMS system resulted in significant inhibition of TC degradation, reducing the removal rate by 32% and 60%, respectively [35,36]. The highest quenching efficacy observed with FFA suggests that the dominant degradation mechanism in the Co_3O_4-*x*/PMS system is a non-radical pathway involving $^1O_2$. Besides, considering that the redox potential of $O_2^{\cdot-}$ is as low as −0.33 V (*vs.* NHE), which is theoretically difficult to effectively degrade TC [37]. The introduction of trace amounts of p-BQ exerted a significant inhibitory effect on the degradation process, suggesting that $O_2^{\cdot-}$ may serve as a key precursor to $^1O_2$ [38].

Moreover, quenching experiments conducted on the pristine Co_3O_4/PMS system revealed the similar trend, indicating the same types of ROS produced (Fig. S9 in Supporting information). However, the inhibitory effect of FFA on the pristine Co_3O_4/PMS system was less pronounced, suggesting a lower contribution of $^1O_2$ compared to Co_3O_4-*x*/PMS system. Therefore, FFA was further employed as a probe to quantitatively determine the steady-state concentrations of $^1O_2$ ($[^1O_2]_{ss}$) generated in each system [39]. As shown in Fig. 3d and Fig. S10 (Supporting information), the Co_3O_4-*x*/PMS system generated significantly higher $[^1O_2]_{ss}$ than Co_3O_4/PMS system, and the amount of $[^1O_2]_{ss}$ positively correlated with the TC degradation performance in each system, which confirmed $^1O_2$ originated from plasma-induced O_v and drived the degradation (Fig. 3e). In addition, the influence of O_2 and N_2 on the degradation reaction can be ignored, thus the path of converting dissolved oxygen to $^1O_2$ was excluded (Fig. S11 in Supporting information) [40]. Based on the above experimental results, it can be inferred that the O_v on the Co_3O_4-*x* surface serve as crucial adsorption sites and electron donors, selectively generating $^1O_2$ *via* PMS activation rather than $SO_4^{\cdot-}$ or $^{\cdot}$OH radicals. Herein, it is speculated that O_v received electrons from PMS and generated $O_2^{\cdot-}$, which functioned dually as intermediates for $^1O_2$ formation and as effective ROS directly attacking TC (Fig. 3f, Eqs. 1–4) [41].

$$O_v + 2HSO_5^- \rightarrow O_2^{\cdot-} + 2HSO_4^- \quad (1)$$

$$O_2^{\cdot-} + H_2O \rightarrow HOO^{\cdot} + OH^- \quad (2)$$

$$O_2^{\cdot-} + HOO^{\cdot} \rightarrow {}^1O_2 + HOO^- \quad (3)$$

$$^1O_2 + TC \rightarrow \text{degradation products} \quad (4)$$

$^1O_2$ typically exhibits high selectivity towards organic compounds containing electron-rich moieties [42]. Therefore, six contaminants with varying electron-donating capacities (methyl orange (MO), sulfamethoxazole (SMX), bisphenol A (BPA), TC, ciprofloxacin (CIP), and benzoic acid (BA)) were selected for investigation [43,44]. As shown in Fig. 4a and Fig. S12 (Supporting information), the Co_3O_4–30/PMS system exhibits significantly higher degradation efficiency for electron-rich organics (MO, SMX, BPA, TC) compared to electron-deficient organics (CIP, BA). The distinct selectivity is attributed to the electrophilic property. Another distinguishing feature of $^1O_2$ is its strong resistance to Inorganic anions. Then, high concentrations of interfering anions ($H_2PO_4^-$, Cl^-, HCO_3^-, NO_3^-, SO_4^{2-}) and humic acid (HA) were introduced (Fig. 4b and Fig. S13 in Supporting information). In the presence of anions, the degradation efficiency of TC remained above 80%. Even with the addition of HA, the removal rate still reached 75%.

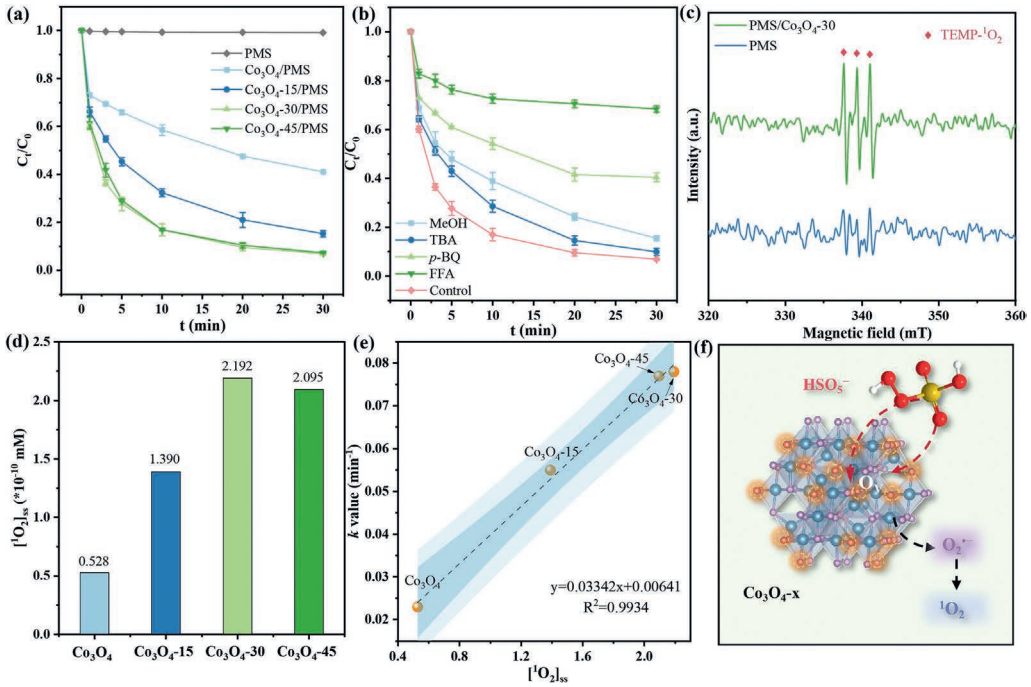


Fig. 3. (a) The degradation efficiency of TC in different reaction systems. (b) Quenching experiments in Co_3O_4–30/PMS system. (c) ESR spectrum of $^1O_2$ in Co_3O_4–30/PMS system. (d) $[^1O_2]$ss in different reaction systems (mM = mmol/L). (e) The relationship between the $[^1O_2]$ss of and k value in different systems. (f) Generation pathway of $^1O_2$ in Co_3O_4-x/PMS systems. Reaction conditions: [catalysts] = 0.2 g/L, [TC] = 20 mg/L, [PMS] = 0.2 g/L, [MeOH] = [TBA] = 100 mmol/L, [*p*-BQ] = 10 mmol/L, [FFA] = 50 mmol/L, pH 7.0.

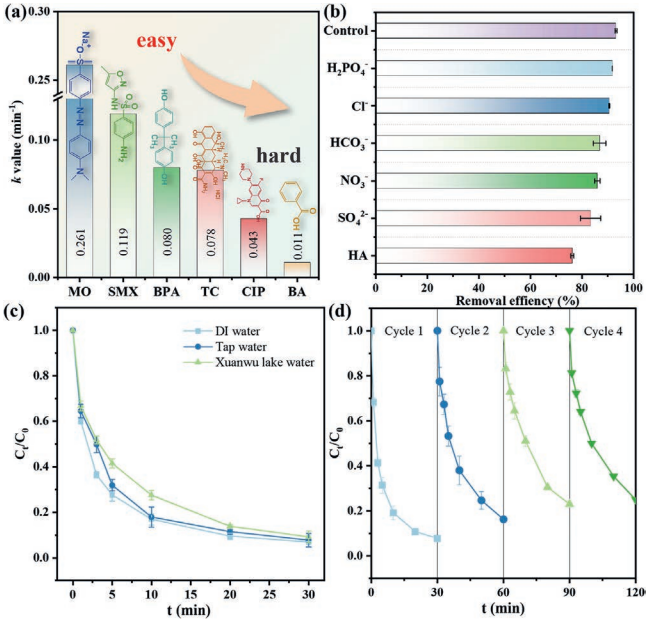


Fig. 4. (a) *k* values of different pollutants in Co_3O_4–30/PMS system. (b) Effect of inorganic ions and HA on TC degradation in Co_3O_4–30/PMS system. (c) Performance of the Co_3O_4–30/PMS system for TC removal in distinct water bodies. (d) TC degradation efficiency over four cycles in Co_3O_4–30/PMS system. Reaction conditions: [catalysts] = 0.2 g/L, [pollutants] = 20 mg/L, [PMS] = 0.2 g/L, [anions] = 50 mmol/L, [HA] = 5 mg/L, pH 7.0.

in TC removal. Overall, the Co_3O_4–30 material demonstrated favorable environmental tolerance. Furthermore, the adaptability of Co_3O_4–30/PMS system was evaluated under realistic water matrices, including tap water and lake water. As depicted in Fig. 4c, the Co_3O_4–30/PMS system maintained high oxidation efficiency in these complex environments, achieving over 90% TC removal within 30 min in both cases. Catalyst recyclability was confirmed over four consecutive cycles, where TC degradation efficiency consistently retained >70%, demonstrating strong durability for pollutant abatement (Fig. 4d). The slight decrease in the removal rate of TC after four cycles may be attributed to the decline of the active sites on the catalyst surface and the catalytic activity of Co_3O_4–30 can be restored through simple plasma treatment. Additionally, the XRD pattern reveals that the characteristic peaks of the catalyst remained consistent before and after the reaction (Fig. S14 in Supporting information), confirming the structural stability of the Co_3O_4–30. Although O 1s XPS analysis shows a slight decrease in the proportion of O_{ads} on cycled Co_3O_4–30, indicating a reduction of O_v, the O_{ads} content remains higher than that of the pristine Co_3O_4 (Fig. S15 in Supporting information). Thus, Co_3O_4–30 maintains relatively high catalytic activity within a certain number of cycles, which can be attributed to its surface-rich O_v. Furthermore, these results provide additional evidence that O_v indeed serves as the key active site for catalyzing PMS to generate $^1O_2$.

In summary, we successfully introduced O_v to the surface of Co_3O_4-*x via* a facile and efficient N_2 plasma treatment strategy. The O_v rich Co_3O_4–30/PMS system achieved 93.2% TC degradation within 30 min ($k = 0.078$ min^{-1}), significantly outperforming the untreated catalyst. The O_v served as key electron acceptors, facilitating the adsorption of PMS to generate the intermediate $O_2^{\bullet-}$, which subsequently which subsequently led to the production of $^1O_2$. Dominated by the $^1O_2$, the Co_3O_4–30/PMS system exhibited strong oxidative degradation capability toward electron-rich pollutants, demonstrating high selectivity in wastewater purification. The system also showed excellent tolerance to high concentrations of interfering ions and organic matter. As the primary technique employed to engineer catalyst defects, plasma treatment offers a simple and controllable approach for enabling non-radical AOPs for selective pollutant degradation, holding significant potential for practical water purification applications.

Declaration of competing interest

The authors declare that they have no known competing financial interests or personal relationships that could have appeared to influence the work reported in this paper.

CRediT authorship contribution statement

Keyi Gao: Writing – original draft, Validation, Methodology, Investigation. **Yunbo Wu:** Writing – original draft, Formal analysis. **Shulin Shen:** Investigation, Data curation. **Dawei Wang:** Writing – review & editing, Supervision, Funding acquisition. **Yilan Jiang:** Writing – review & editing, Supervision, Funding acquisition.

Acknowledgments

We would like to thank the financial support from Fundamental Research Funds for the Central Universities (No. B250201030), the National Natural Science Foundation of China (Nos. 52370072, 52400031, 52325003), and the Natural Science Foundation of Jiangsu Province (No. BK20242057).

Supplementary materials

Supplementary material associated with this article can be found, in the online version, at doi:10.1016/j.cclet.2025.112286.

References

[1] H.K. Allen, J. Donato, H.H. Wang, et al., Nat. Rev. Microbiol. 8 (2010) 251–259.
[2] D.G.J. Larsson, C.F. Flach, Nat. Rev. Microbiol. 20 (2022) 257–269.
[3] D.B. Miklos, C. Remy, M. Jekel, et al., Water Res. 139 (2018) 118–131.
[4] K. Yin, Y. Tang, Z. Li, et al., Water Res. 285 (2025) 124130.
[5] F.N. Anandraj, T.K. Panda, S. Thangarasu, G. Palanisamy, K.E. Neerugatti, Water Res. 284 (2025) 123941.
[6] S. Giannakis, K.Y.A. Lin, F. Ghanbari, Chem. Eng. J. 406 (2021) 127083.
[7] J. Zhen, J. Sun, X. Xu, et al., Angew. Chem. Int. Ed. 63 (2024) e202402669.
[8] P.V. Nidheesh, G. Boczkaj, S.O. Ganiyu, et al., Environ. Chem. Lett. 23 (2025) 195–240.
[9] H. Deng, N. Zhao, J. You, et al., Chin. Chem. Lett. 36 (2025) 110650.
[10] Y. Jiang, K. Gao, T. Chen, et al., Chem. Eng. J. 500 (2024) 156532.
[11] Y. Jiang, K. Gao, Y. Li, et al., Chem. Commun. 60 (2024) 3158–3161.
[12] J. Qin, Q. Wang, B. Han, et al., Appl. Catal. B 360 (2025) 124538.
[13] Y. Wang, Y. Lin, S. He, S. Wu, C. Yang, J. Hazard. Mater. 461 (2024) 132538.
[14] L. Lai, H. Zhou, Y. Hong, et al., Chin. Chem. Lett. 35 (2024) 108580.
[15] J. Zhang, D. Yan, G. Ding, et al., Angew. Chem. Int. Ed. 64 (2025) e202511448.
[16] X. He, F. Marken, A. Vertova, A. Minguzzi, J. Environ. Manage. 385 (2025) 125583.
[17] Z. Chen, G. Ding, Z. Wang, et al., Adv. Funct. Mater. 35 (2025) 2423213.
[18] N. Nippatlapalli, A. Ganta, Process Saf. Environ. Prot. 187 (2024) 1454–1470.
[19] Z. Ye, L. Zhao, A. Nikiforov, et al., Adv. Colloid Interface Sci. 308 (2022) 102755.
[20] C. Li, B. Ye, B. Ouyang, et al., Adv. Mater. 37 (2025) 2501381.
[21] Y. Xie, Y. Feng, S. Zhu, et al., Adv. Mater. 37 (2025) 2414801.
[22] K. Wang, T. Zhao, N.Q. Ren, S.H. Ho, Water Res. 265 (2024) 122304.
[23] X. Wang, M. Wu, B. Liu, et al., Chem. Eng. J. 519 (2025) 165473.
[24] J. Zou, Y. Zou, H. Wang, et al., Chin. Chem. Lett. 34 (2023) 107378.
[25] Y. Chen, Q. Li, R. Su, et al., Water Res. 282 (2025) 123765.
[26] S. Wang, J. Kang, P. Yan, et al., Appl. Catal. B 342 (2024) 123419.
[27] G. Zhu, W. Tan, T. Gu, A. Dou, Q. Xu, Appl. Surf. Sci. 709 (2025) 163742.
[28] G. Ding, J. Zhang, D. Yan, et al., Nano Lett. 25 (2025) 8984–8992.
[29] Y. Xiao, G. Ding, J. Tao, et al., Nat. Commun. 16 (2025) 7476.
[30] J. Hu, B. Qian, X. Zeng, et al., J. Mater. Chem. A 9 (2021) 16489–16499.
[31] L. Gao, Y. Guo, J. Zhan, G. Yu, Y. Wang, Water Res. 221 (2022) 118730.
[32] Z. Chen, D. Yan, X. Wang, et al., ACS Catal. 15 (2025) 13568–13580.
[33] H. Han, M. Chen, C. Sun, et al., Water Res. 268 (2025) 122666.
[34] K. Yin, J. Yang, Y. Li, Q. Li, X. Xu, Chin. Chem. Lett. 35 (2024) 109847.
[35] X. Li, X. Zhang, J. Lang, et al., Sci. Bull. 69 (2024) 3867–3875.
[36] Y. Guo, J. Long, J. Huang, G. Yu, Y. Wang, Water Res. 215 (2022) 118275.
[37] L. Wu, Z. Sun, Y. Zhen, et al., Environ. Sci. Technol. 55 (2021) 15400–15411.
[38] Q. Fang, H. Yang, S. Ye, et al., Water Res. 245 (2023) 120614.
[39] H. Wang, D. Wang, C. Sun, et al., Appl. Catal. B 364 (2025) 124854.
[40] Y. Yao, J. Zhang, Y. Wang, et al., Chin. Chem. Lett. 35 (2024) 109633.
[41] S.H. Zhou, R.D. Wang, Y. Yang, et al., Chem. Eng. J. 513 (2025) 163031.
[42] Y. Zhao, L. Yu, C. Song, et al., Environ. Sci. Technol. 56 (2022) 10710–10720.
[43] M. Ao, J. Wei, C.S. He, et al., Chin. Chem. Lett. 36 (2025) 109882.
[44] C. Jin, B. Han, C. Luo, et al., Water Res. 287 (2025) 124420.